Full length article

Harvesting superior intrinsic plasticity in nitride ceramics with negative stacking fault energy

Yong Huang [a], Zhuo Chen [a], Michael Meindlhumer [b], Rainer Hahn [c], David Holec [b], Thomas Leiner [b], Verena Maier-Kiener [b], Yonghui Zheng [d], Zequn Zhang [a], Lukas Hatzenbichler [b], Helmut Riedl [c], Christian Mitterer [b], Zaoli Zhang [a,*]

[a] Erich Schmid Institute of Materials Science, Austrian Academy of Sciences, Jahnstraße 12, Leoben A-8700, Austria
[b] Department of Materials Science, Montanuniversität Leoben, Franz-Josef-Strasse 18, Leoben A-8700, Austria
[c] Christian Doppler Laboratory for Surface Engineering of high-performance Components, TU Wien A-1060, Austria
[d] Key Laboratory of Polar Materials and Devices (MOE), Department of Electronics, East China Normal University, Shanghai 200241, PR China

ARTICLE INFO

ABSTRACT

Ceramics face an everlasting challenge from their intrinsic brittleness at room temperature, which can lead to early-stage catastrophic failures. The fatal disadvantage primarily results from the high critical-resolved shear stress required to initiate dislocation movement and the limited number of operational slip systems. Here, we propose a new strategy for designing deformable ceramics by negative stacking fault energy (SFE), which realizes energetic barrier reduction of dislocation motion and slip system expansion. This way, we harvested a superior room-temperature compressive plasticity in TiN/TaN superlattice by successive and extensive atomic plane faulting and twinning. This strategy sheds light on the design of intrinsically ductile ceramics.

1. Introduction

Ceramic materials exhibit several advantages over metals, including superior hardness, wear resistance, thermal stability, and oxidation resistance [1–3]. Nevertheless, their intrinsic brittleness significantly restricts broader applications of ceramics. According to the theory of dislocations [4], dislocations are the main carriers of plastic deformation in crystalline solids and are crucial in stress relaxation. However, strong covalent and ionic bonds in ceramic materials cause extremely high critical resolved shear stress, which impedes the nucleation of dislocations [5]. Additionally, the motion of dislocations in ceramics is significantly constrained due to the limited number of slip systems [6]. Consequently, the scarcity of pre-existing dislocations and severely restricted mobility of dislocations results in the well-documented brittleness of ceramics at ambient temperature.

To enhance deformability and damage tolerance, researchers have extensively explored the deformation mechanism of ceramics to achieve considerable plastic deformation. Since investigations into zirconia-based ceramics, phase transformation-induced toughening has been a focal point [7]. Recently, more promising systems arose for remarkable mechanical property enhancement through bonding switches and phase transformation [8,9]. Besides, decoupling deformation from dislocations, such as viscous creep and shear band slip propagation in amorphous oxides [10] and unit-cell disturbances in $WN_{0.5}$ [11], also significantly enhanced mechanical properties. Moreover, the challenge of dislocation nucleation during deformation can be relieved by introducing pre-existing defects. Flash-sintering [12,13] and mechanical deformation [14–16] have shown potential for tuning dislocation density and improved deformability to some extent. In the thin film fields, misfit dislocation arrays through lattice mismatch and artificial interfaces have been proven to effectively enhance strength and fracture toughness [17–19]. Besides, introducing a metal phase can decrease the threshold for dislocation nucleation and promote the dislocation motion during deformation [20–22]. However, these proposed routes are somewhat uncontrollable or may limit the strength of the failure. Challenges such as stringent synthesis processes and limited generalizability of the method remain. More importantly, all these methods cannot fundamentally and intrinsically change the brittleness of ceramics.

To intrinsically improve the room-temperature plasticity of ceramics, reducing the threshold of plastic deformation and expanding the slip system are essential and required in the long run. Inspired by

---

transformation-induced plasticity and twinning-induced plasticity in steels [23,24], we propose a new strategy to fundamentally change the brittleness of the ceramic, i.e., by applying ceramics with lower stacking fault energy (SFE) or a negative SFE. Despite the common belief that ceramics generally exhibit high stacking fault energies (SFEs) due to their strong ionic and covalent bonds, making the formation of stacking faults (SFs) and twinning challenging, transition metal nitrides (TMNs)—particularly those in the VB and VIB groups of Periodical Table, as well as various high entropy nitrides [25,26]—defy this stereotype by exhibiting negative SFEs. These TMNs are known for their role as hard protective coatings. Negative SFE is associated with unique deformation mechanisms and superior mechanical properties [27,28]. It indicates a strong tendency of dissociation into partial dislocations, and the reduced energy landscape of the generalized stacking fault energy (GSFE) curve significantly influences dislocation motion, facilitating deformation-induced twinning and phase transformation [29–31]. Our previous studies have proved the feasibility of introducing high-density SFs into TaN [32]. By tuning the bilayer period of TiN/TaN multilayers, the hardness shows a synchronous variation trend with the SF density. However, the detailed deformation mechanism behind the strengthening and its influence on the ductility still lack systematic investigations. This work showcases a TiN/TaN superlattice with each layer thickness of 50 nm. We found that only this structure produced a fully epitaxial multilayer. Thinner laminate thicknesses like 10 nm can produce a higher density of SFs, but they will also introduce columnar grain boundaries and other growth orientation textures because of polycrystalline [32]. To better understand the deformation mechanism of such superlattice and exclude the influence of columnar grain boundaries and textures, we chose the laminate thickness of 50 nm as a model. Assisted by density function theory (DFT) and aberration-corrected transmission electron microscopy (TEM), we predict and prove the various SF configurations. Next, by combining *in-situ* micro-mechanic tests and post-mortem TEM observations, we reveal an excellent combination of room-temperature plasticity, strength, and toughness of such ceramic superlattice, and track its deformation mechanism down to atomic scale.

2. Materials and methods

2.1. The synthesis method of the film

The film used in this study was prepared by direct current magnetron sputtering using a custom-made lab-scale magnetron sputter deposition system equipped with a Ti target (99.99 % purity, ⌀ 50.8 mm × 6 mm) and a Ta target (99.99 % purity, ⌀ 50.8 mm × 6 mm). The film was grown on MgO(001) substrate at 700 °C, and the substrate potential was kept floating during the deposition. Besides, the partial pressure of N_2 and Ar was kept at 0.2 Pa and 0.6 Pa, respectively. The multilayer structure was achieved by computer-controlled shutters in front of the targets. The nominal thickness for TiN and TaN was set to be 50 nm for both. The superlattice starts with the TiN layer and ends with the TaN layer.

2.2. X-ray diffraction measurement

The overall composition and crystallographic structure of the films were characterized by X-ray diffraction (XRD) using Bruker D2 Phaser X-ray diffractometer with Co Kα radiation with a wavelength of 1.790Å (operated at 30 kV and 10 mA). Samples were placed on a silicon wafer to minimize the background influence. The diffraction was conducted in the range from 15° to 70° at a scanning rate of 1.625°/min.

2.3. Nanoindentation test

Indentation tests were conducted on a KLA Nanoindenter G200 equipped with a diamond cube-corner indenter tip (Synton-MDP) to obtain hardness H and Young's Modulus E by the conventional analysis first proposed by Oliver and Pharr [33]. The tests applied the continuous stiffness measurement method with a superimposed sinusoidal signal (2 nm, 45 Hz) and a constant indentation strain rate ε of 0.05 s^{-1}. Six indentations were performed at each displacement (100 nm, 300 nm, 500 nm) for mechanical property measurement.

2.4. TEM sample preparation

The cross-sectional TEM lamella of the as-deposited and indented films was machined by focused ion beam (FIB) using an FEI Helios NanoLab 660 workstation. The residual impression with the largest displacement over the film thickness was chosen to be cut. On the other hand, a large indentation depth would introduce cracks so that we can investigate the crack propagation. On the other hand, a shallow indentation impression is usually hard to maintain during FIB milling. Before the FIB cutting, a 3-micron protective carbon layer was deposited on the residual impression. And the lamella was cutting along the ⟨110⟩ direction of the substrate. Trenches were cut at 9 nA, and cross sections were cleaned at 2 nA. Then, the lamella was cut and transferred to a Cu TEM grid. The lamella was polished using accelerating voltages from 30 to 2 kV and ion currents ranging from 20 nA to 7 pA.

2.5. TEM characterization

For high-resolution TEM (HRTEM) characterization, JEOL 2100F and FEI Titan Themis 60–300 cubed TEM that are both equipped with an image-side spherical aberration (Cs) corrector (CEOS GmbH) were adopted. The aberration coefficients were set to be sufficiently small before investigations.. Scanning TEM (STEM) images in this study were acquired by a 300 kV field emission TEM (JEOL ARM300F) equipped with double Cs-correctors. High-angle annular dark-field (HAADF) images were acquired with the camera length set as 73 mm, and the collection angle range of the ADF detector is about 79.5–200 mrad. Energy-dispersive X-ray spectra (EDXS) were acquired by JEOL ARM300F equipped with double Cs-correctors or FEI Titan Themis 60–300 cubed TEM (operated at 300 keV). The JEOL ARM300F is equipped with two windowless detectors, each of which has an active area of 100 mm2. The FEI Titan Themis is equipped with a SUPER-X spectrometer with 4 SDD windowless detectors. The composition quantification was conducted using the k-factor method after peak fitting.

2.6. Micromechanical tests

In-situ micromechanical tests were carried out in a ZEISS LEO 982 SEM equipped with a Hysitron PI 85 nanoindenter. At first, the as-deposited sample was ground into a wedge shape and the thinner side was immersed in H_2SO_4 solution (0.5 mol/L) to dissolve the MgO substrate. Then 5 cantilevers of $10 \times 2 \times 1.2$ μm^3 from the as-deposited film were prepared by FIB at 30 keV using an FEI Helios NanoLab 660 workstation. A set of milling currents ranging from 2 nA for rough shaping down to 40 pA for final polishing. In order to determine the fracture toughness K_{IC} of the film, a pre-notch with a depth of about 300 nm was manufactured using a current of 7 pA for 20 s. The experiments were conducted using a Hysitron PI85 (Bruker Corporation, Billerica, Mass., USA). The samples were loaded and fractured using a sphere-conical indenter tip (Synton MDP AG, Switzerland) with a tip radius of 700 nm using a loading speed of 20 nm/s applied in a displacement-controlled feedback loop. The received load (P)-deflection (ω) curves were corrected for instrument compliance. The maximum recorded force F_f at failure and the actual dimensions of the fracture surface measured by SEM (Leo 1525, Zeiss) were all used to derive a value for the critical stress intensity K_{IC} (in MPa$\sqrt{m}$) for each cantilever. From the maximum applied load at fracture P_{max}, the fracture stress σ_F was calculated according to

$$\sigma_{\mathrm{F}} = 6\frac{P_{\max}L}{Bt^2} \tag{1}$$

where *B, L* and *t* are the width, the length, and the thickness of the cantilever, respectively.

By applying linear elastic fracture mechanics, K_{IC} was calculated as

$$K_{\mathrm{IC}} = \sigma_{\mathrm{F}}\sqrt{\pi a} \times Y\left(\frac{a}{t}\right) \tag{2}$$

where $Y\left(\frac{a}{t}\right)$ is the dimensionless shape factor derived by Ref. [34] for the free-standing cantilever geometry.

$$Y\left(\frac{a}{t}\right) = \sqrt{\frac{2t}{\pi a}\tan\left(\frac{\pi a}{2t}\right)}\ \frac{0.923 + 0.199\left(1 - \sin\left(\frac{\pi a}{2t}\right)\right)^4}{\cos\left(\frac{\pi a}{2t}\right)} \tag{3}$$

The measurements of parameters *a, B, L*, and *t* can be found in Fig. 6.

Micro-pillar geometries for compression tests were produced by a focused ion beam (FIB) using a ThermoFisher Scios 2 FIB-SEM instrument. The micropillars' aspect ratio was about 1.6, with a diameter of about 800 nm [35]. The geometries were prepared using a Ga-ion probe current of 7 nA for the rough cut down to 50 pA for the finishing step. Special attention was given to stopping the milling process directly at the coating-substrate interface.

The pillar compression tests were performed in a Zeiss Sigma 500 VP system combined with a FemtoTools FT-NMT04 in-situ SEM nano-indenter equipped with a flat punch (5 μm diameter) diamond tip capable of applying 200 mN at a noise level of < 5 μN (measured at 10 Hz). The tests were carried out at room temperature in displacement-controlled mode with a displacement rate of 5 nm/s. The recorded load-displacement curves were used to calculate the engineering stress following an approach by Wheeler and Michler [36], where the top diameter of the pillar is taken as the reference contact area. The engineering strain was obtained from the displacement data using the coating thickness as the initial pillar height reference. Moreover, the displacement data was corrected by accounting for the base compliance following Sneddon's correction [37] given by:

$$\Delta L = \frac{1 - \nu_{sub}^2}{E_{sub}} * \frac{F}{d}$$

where ν_{Sub} and E_{Sub} are the Poisson's ratio and Young's modulus of the substrate, respectively, $\nu_{sub} = 0.18$, $E_{sub} = 291$ GPa [38]. *F* is the applied force, and *d* is the diameter of the pillars. ΔL is then the deformation of the substrate induced by the pillar and must be subtracted before calculating the strain.

2.7. Ab initio calculations

The computations were conducted utilizing the Vienna ab-initio Simulation Package (VASP) [39], employing the projector-augmented wave (PAW) approach along with a plane wave basis set [40]. Generalized gradient approximation (GGA) functionals from Perdew-Burke-Ernzerhof (PBE) [41] were employed to handle exchange-correlation effects. The k-point grid used for this study was a Monkhorst-Pack [42] $10\times10\times2$ mesh and the plane wave cut-off energy was set to 600 eV We used a full structural relaxation for the B1 structure. Afterwards, we built models for calculating stacking faults during which only the atomic positions were allowed to relax. As a structural unit, we used model composed of 6 {111} planes (3 metals and 3 N atoms) [43]. Subsequently, we created a $1\times1\times4$ supercell, thereby containing 12 metal {111} planes and 12 N {111} planes. Next, we applied a shear displacement along the <11−2> direction by tilting the supercell lattice vector c (along the original [111] direction), while initially keeping the atomic Cartesian coordinates unchanged w.r.t. the undeformed supercell. This way, a SF every 24 {111} planes was

introduced into our model, allowing calculating the GSFE profile by gradually increasing the tilt into the $\langle 11–2 \rangle$ direction.

3. Results and discussions

3.1. Ab initio calculations

First, we calculated and compared the GSFE curves (Fig. 1a, b) along $\langle 11\overline{2} \rangle$ direction for TiN and TaN and we found the peculiarity of TaN and its effect on the deformation behavior at the atomic level. Unlike metals, the alternating stacking of cation and anion layers of ceramics creates more configurations for SFs in ceramics [44]. DFT calculation yielded curves for both stable B1 TMNs with two local minima. Fig. 1c illustrates the different configurations of SFs where ABC and αβγ represent the stacking sequence of metal and nitrogen layers, respectively. The first local minimum is usually referred to as the lowest SF (LSF) due to its lowest SFE. The second local minimum is known as intrinsic SF (ISF), characterized by a ball-on-ball configuration of a nitrogen layer exactly over a transition metal layer (i.e., αCβAγB/βAγBαC). Besides, Two alternative configurations further decrease the energetic barrier at a/3⟨11$\overline{2}$⟩ displacement, which is achieved by the cooperative motion of a nitrogen or metal layer next to the SF [45]. If the nitrogen layer moves back (AγB/αCβ→AγB/γAγ), it results in a configuration called "synchro metal". Conversely, the movement of the metal layer (AγB/αCβ→AγB/αBγ) leads to the "synchro N" configuration. According to the GSFE curve of TaN (Fig. 1b), both SFEs for the LSF and the synchro metal configuration are negative, which means ⟨11$\overline{2}$⟩{111} is the energetically preferred slip system for TaN. The operation of the ⟨11$\overline{2}$⟩ {111} slip system in TaN allows for more active slip systems. In contrast, due to a much higher SFE and to prevent shearing planes from bringing the same charge sign ions too close, TiN tends to glide along <110> {110} at ambient temperature [45,46]. This leads to a very limited number of slip systems and intrinsic brittleness for TiN. Besides, the stress required to activate the dislocation gliding in TaN is much lower than in TiN. The maximum stress values (τ) computed from the slope of GSFE curves indicate that $\tau_{\langle 11\overline{2}\rangle\ \{111\}}$ of TaN (12.5 GPa) is much smaller than $\tau_{\langle 110\rangle\ \{110\}}$ of both TiN (21.2 GPa) and TaN(29.2 GPa) [47]. These determined the intrinsic ductility of TaN. Additionally, negative SFEs make partial dislocations to avoid accumulation on the adjacent layers and minimize the system's energy. Otherwise, successive SFs on the neighboring layers will result in two coherent twin boundaries, reducing the faulted layers in the face-centered cubic matrix [31]. Thus, extensive faulting rather than twin transformation is preferred for TaN and could effectively prevent strain localization. These calculations and predictions lay a solid foundation for achieving room-temperature ductility in nitride ceramics.

3.2. Characterization of as-deposited superlattice

We then constructed a TiN/TaN superlattice grown on MgO (100) substrate with a 1270 nm thickness by physical vapor deposition. XRD pattern of as-deposited TiN/TaN (Fig. 2a) indicate that the superlattice consists of rock-salt structure TiN and TaN that are grown epitaxially along MgO [002]. On the other hand, STEM EDX mapping is shown in Fig. 2b - d. Quantification result shows that compositions of TaN and TiN are (41.33±6.57 at.% N and 58.67±11.27 at.% Ta), (43.84±7.48 at. % N and 56.16±12.12 at.% Ti) respectively. An overview morphology is shown in the high-angle annular dark-field (HAADF) scanning transmission electron microscopy (STEM) image (Fig. 3a). The selected area electron diffraction (SAED) pattern indicated that there is a good epitaxy between the two layers. The local magnified HAADF STEM image indicates a relatively sharp and flat interface between the two layers, and the original thickness of TaN and TiN are about 45 and 38 nm, respectively. The bright field (BF) STEM image in Fig. 3b shows plenty of straight pre-existing SFs whose density is about $1.9\times10^{15}/\mathrm{m}^2$ within the
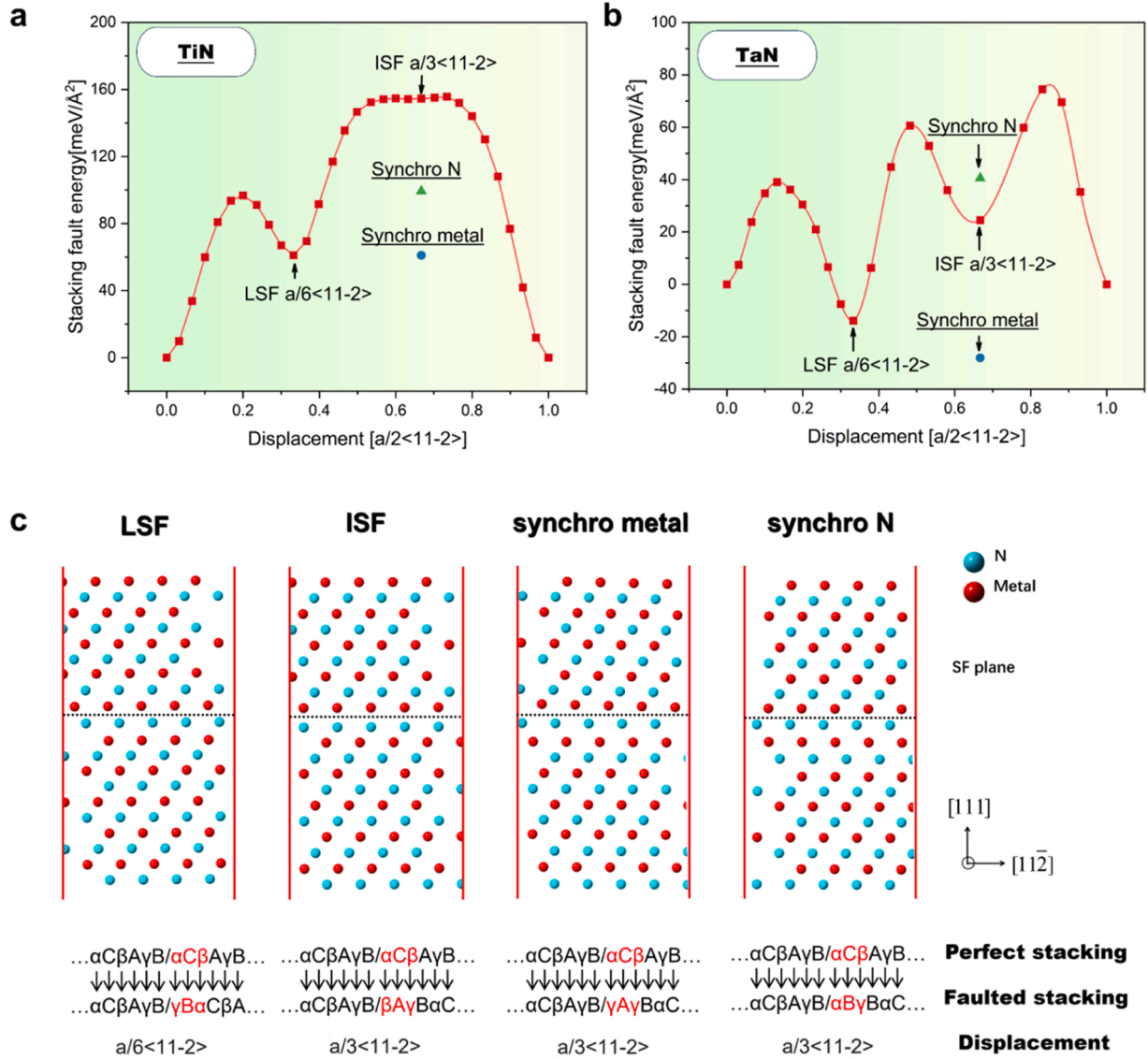
Fig. 1. GSFE curves of TiN and TaN and different configurations of TaN. The GSF energies of TiN and TaN as a function of the shear displacement in the {111} planes along the $\langle 11\bar{2} \rangle$ direction, there are two local minima for **(a)** TiN and **(b)** TaN, corresponding to LSF at $1/6\langle 11\bar{2} \rangle$ and ISF at $1/3\langle 11\bar{2} \rangle$. Besides, two more SFs induced by synchronous shearing are also at $1/3\langle 11\bar{2} \rangle$. **(c)** Atomic models and stacking orders of different SF configurations with their corresponding shear displacements.

TaN layer. As discussed in the previous work [32], these SFs mostly resulted from the dissociation of misfit dislocation arrays, which can be described as $\frac{a}{2}[110] \rightarrow \frac{a}{6}[21\bar{1}] + \frac{a}{6}[121]$. The high-resolution TEM (HRTEM) images in Fig. 3**c** - **f** display the atomic structure of these defects. Aberration-corrected TEM enables distinguishing actual SF configurations. As predicted above, four kinds of SFs were all identified in the as-deposited film (Fig. 3**d** - **f**). The diversity of SF configuration provides partial dislocations with an adaptive displacement freedom. DFT calculation also predicted that Ta vacancies are preferable in B1 TaN [48], and a darker contrast of SFs was observed in HAADF image like Fig. 3**g**. To investigate whether there is an aggregation of Ta vacancies near the SF, atomic-scale EDXS was conducted (Fig. 3**h** - **k**). The line scan of Ta intensity in Fig. 3**h, l** shows no compositional difference across the SF. Although a weak fluctuating signal from Ti was observed, concentration quantification indicates that Ti accounted for only 3 at.% compared to Ta. Given that Ti and Ta targets were powered during deposition, it is likely that some of the lighter Ti atoms, compared to Ta, were scattered, and not efficiently shielded by the shutter. Thus, the possibility of metal vacancy aggregation from the contrast variation can be ruled out.

3.3. Mechanical properties

To evaluate the room temperature plasticity, we conducted uniaxial micropillar compression tests. Fig. 4**a** summarizes typical micropillar compression results and corresponding strain-stress curves. The circumstance for most ceramics is a brittle failure, where the pillars fail catastrophically shortly after yielding with minimal or unnoticeable plastic deformation. The second case is the localized plastic deformation, which is usually realized by shear or slip bands. Its curve is distinguished by cyclic sudden stress drops, also known as stress burst, which usually corresponds to slipping of accumulated dislocations [49]. The ideal case is the uniform deformation, characterized by gradual strain hardening and steadily growing stress.

Room-temperature uniaxial micropillar compression tests demonstrate the superior plasticity of the TiN/TaN superlattice. Five testing curves of the superlattice are presented in Fig. 4**b**. During deformation, the pillars experienced reversible elastic strains at first. With the yield
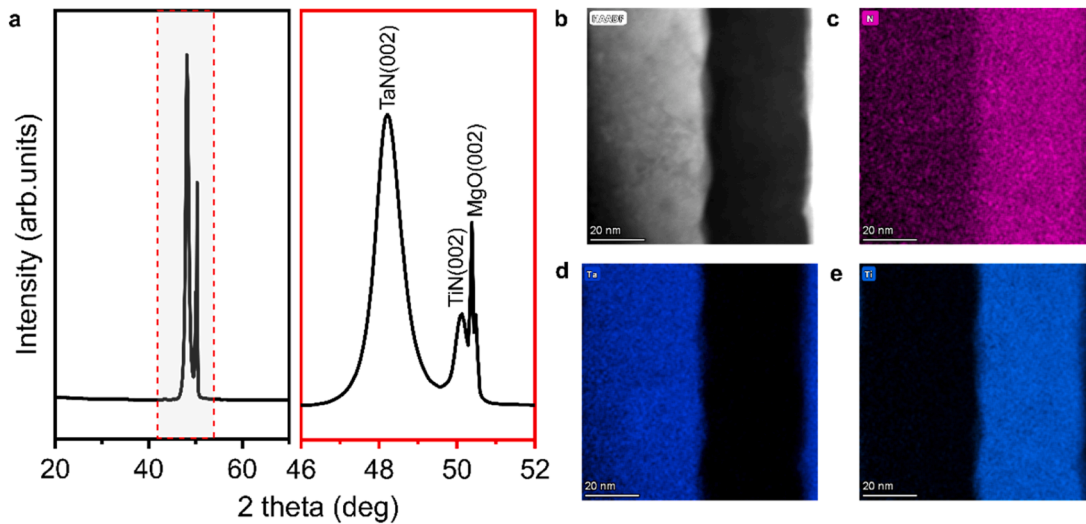
Fig. 2. Phase constitution and composition of as-deposited TiN/TaN superlattice. (a) XRD pattern of as-deposited TiN/TaN. **(b)-(e)** STEM EDX mapping images of N, Ta, and Ti, respectively, in the adjacent TiN and TaN layers.

strength set as the stress value at 0.2% strain offset, plastic yielding initiated irreversible strain when the engineering strain increased to 2.78 ± 0.52 % and the engineering stress reached 7.48 ± 0.62 GPa. Detailed parameters acquired for each pillar are listed in Table 1. Unlike most ceramics, all TiN/TaN pillars exhibit surprising plastic deformability and smooth strain-stress curves. Post-mortem SEM images (Fig. 5) indicate no crack formation for these pillars even after a 43.3% compressive strain. The measurements show the barreling in shapes and obvious increases in the top-surface area. Moreover, these pillars maintain the load-bearing capacity even at $\varepsilon_c \approx 70\%$ (Fig. 4, **b** to **d**). Fig. 4**d** shows a typical cross-section morphology of the pillar ($\varepsilon_c \approx 70\%$), the pillar height reduces from 1270 nm to approximately 410 nm, and some TaN layers' thicknesses reduce by about 90%. Furthermore, a dramatic growth in engineering stress over three times reveals the great potential of strain hardening. We compared the recent room-temperature micropillar compression tests of ceramics (Fig. 4**e**), and this work achieved record-high room-temperature plasticity among ceramics. The TiN/TaN superlattice shows nearly four times better deformability than monolithic TiN. Compared to those using flash-sintering and pre-deformation, our work does not require additional treatment after deposition. More importantly, being non-destructive and homogeneous makes it more applicable. Meanwhile, compared to ductile amorphous oxides [10,50], the synthesis of such superlattice is simpler, and noteworthy strain strengthening makes it more resistant to further loading.

Thanks to the substantial plasticity and strain hardening, a synergistic enhancement of hardness and fracture toughness was also realized. The hardness and elastic modulus were measured as 39.02 ± 1.37 GPa and 413 ± 11.6 GPa, respectively, by nanoindentation experiments (Fig. 6**a** - **c**). Additionally, nanoindentation pile-up from residual impressions (the inset in Fig. 6**a**) also indicate that TiN/TaN can also exhibit good plasticity under nanoindentation. Next, we performed bending tests on free-standing micro-cantilevers with notches to evaluate the impact of improved plasticity on the fracture toughness (Fig. 6**d** - **f**). The obtained fracture toughness shows that the K_{IC} of TiN/TaN superlattice is (3.4 ± 0.5) MPa$\sqrt{m}$, achieving 20% enhancement compared with TiN. By comparing fracture toughness and hardness of recently reported TMN systems (Fig. 6**g**), the introduction of a negative SFE layer into the ceramic superlattice realizes exceptional room-temperature plasticity, strength, and fracture toughness simultaneously.

3.4. Deformation mechanism

To elucidate the origin of the superior mechanical properties, particularly the room-temperature plasticity of the TiN/TaN superlattice, we track the unique deformation mechanisms of TaN layer and the synergistic deformation of the superlattice by gaining insight into the microstructures of post-deformation samples down to the atomic scale.

3.4.1. Deformation dominated by partial dislocations in TaN

BF and HRTEM images in Fig. 7**a, b** present the structure and SFs' density evolution after the deformation. To elucidate the dependence of the SF density on the strain quantitively, we divided the region of interest into three parts (X, Y, and Z). Then, we measured their nominal strain (ε) based on the thickness variation compared to the as-deposited state. The resulting SF density shows a monotonous trend, which can be approximated by a linear dependence on the strain (Fig. 7**b**). More details of the structural evolution of SFs are displayed in Figs. 7**c**. As SF density increases, partial dislocations gliding on different {111} planes interact with others, generating sessile dislocations and jogs. As the spacing between neighboring SFs decreased, more partial dislocations were confined within the blocks bounded by SFs. Concurrently, partial dislocations began to glide on the adjacent planes, creating twin nuclei. When the local strain further increased, the atomic configuration of SFs also began to evolve. The local enlarged part of SFs within the red rectangles shows that the stacking sequence of Ta layers transforms from ABC to CCC (Fig. 7**d**). Meanwhile, the deformation induced substantial distortions in the TaN matrix and SFs. As depicted in Fig. 7**e**, dispersed atomic spacing along $[11\bar{2}]$ indicates a larger displacement freedom for partial dislocations. Additionally, abundant crossing SFs divide the TaN layer into smaller blocks (Fig. 7**f**). Meanwhile, geometric phase analysis (Fig. 7**g**) indicates that these smaller blocks realize gradual on-axis rotation across block boundaries. Fig. 7**h** reveals that these block boundaries consist of narrow twinning bands that result from the accumulation of adjacent partial dislocations. These $\Sigma3\{111\}$ twins not only accommodate large strains but also achieve a gradual orientation change. As marked by the Burgers circuit in Fig. 7**h**, the connection zone of the twinning band typically consists of dislocations with [001] components, which mediates the rotation of (001) planes of these blocks. Consequently, deformation-induced SFs and twinning achieve the superior plastic deformation of TaN.
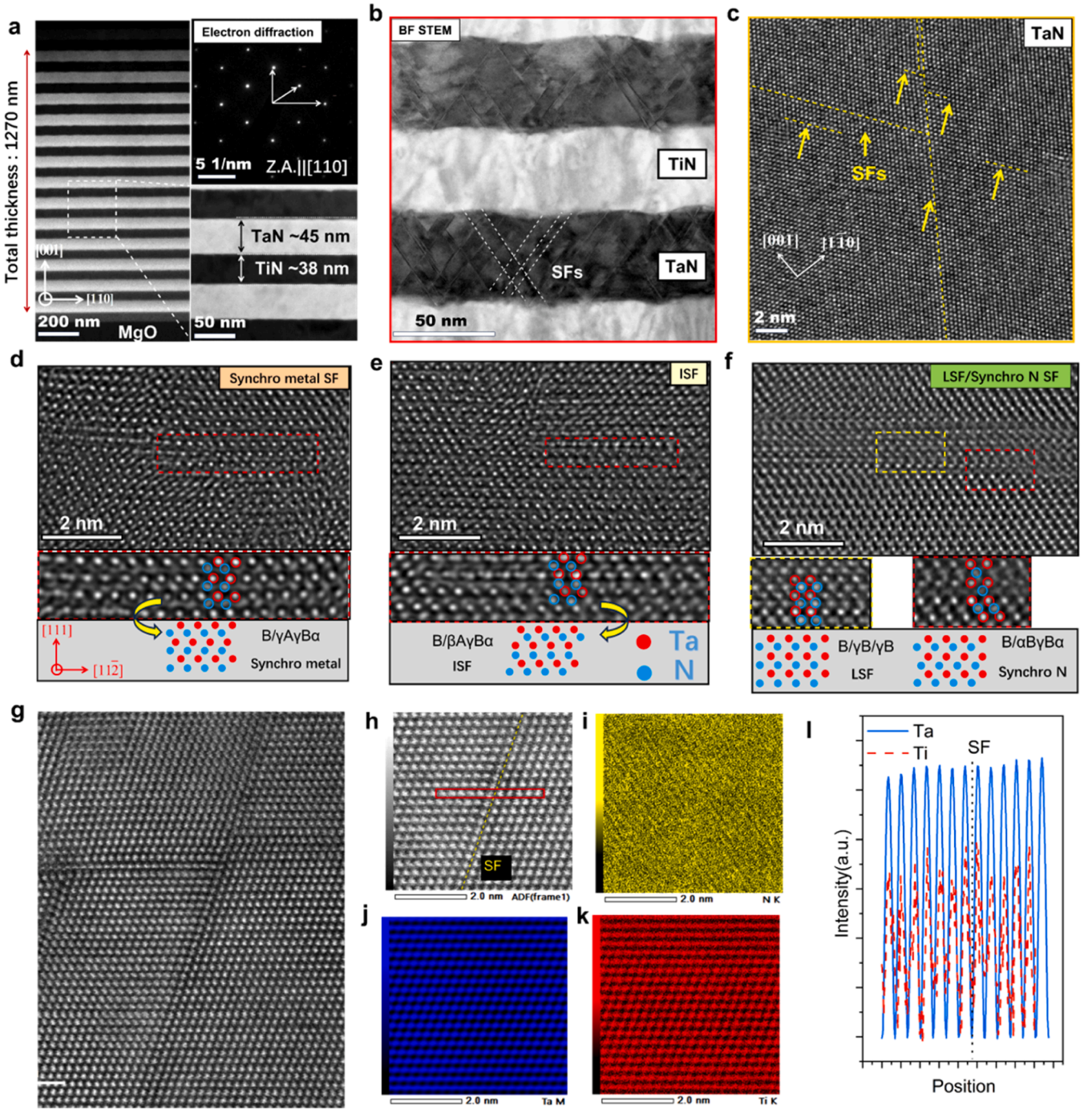
Fig. 3. Microstructure of the as-deposited TiN/TaN superlattice. (**a**) HAADF STEM image of the whole TiN/TaN superlattice viewed along [110] zone axis, in which the bright-contrast layer is TaN. SAED pattern of the superlattice contains nearly coincident diffraction spots, indicating a good epitaxy between adjacent TiN and TaN. The locally magnified HAADF image shows the original thickness of individual layers. (**b**) The BF STEM image shows the dense SFs inside TaN. (**c**) HRTEM image of SFs inside TaN, (**d-f**) Direct imaging of N atomic columns in HRTEM images reveal different configurations of SFs in the as-deposited TiN/TaN superlattice, and corresponding atomic models were highlighted. (**g**) Atomic-resolution STEM EDX mapping images of N, Ta, and Ti, respectively, across an SF. Line profile of signal intensities of Ta and Ti distribution across the SFs shows that there is no observable composition variation across the SF, the position of the SF is marked in Fig. 3h.

3.4.2. Synergistic deformation of TiN/TaN multilayer

The multilayer system introduces abundant mismatch interfaces between TiN and TaN, as well as a high density of pre-existing SFs in the as-deposited state. These interfaces can provide more nucleation sites for subsequent partial dislocations during deformation and pre-existing SFs can also promote the deformability of TaN. However, it cannot fully explain the superior deformability of TiN/TaN, especially when TiN experienced nearly equivalent strains, as shown in Fig. 4d. The

surprising plasticity of TiN within the multilayer system, in our opinion, mainly comes from the synergistic deformation of the multilayer system and the de-accumulation of dislocations. Firstly, the Peierls stress for a/2 <110>{110} dislocation in TiN calculated by DFT is about 1.3–1.4 GPa [80], which is much lower than its critical fracture stress. The main obstacle to its plastic deformation is the nucleation of dislocations. The existence of a ductile TaN layer dramatically decreases the threshold of the dislocation nucleation and acts as a dislocation source or 'seeding'
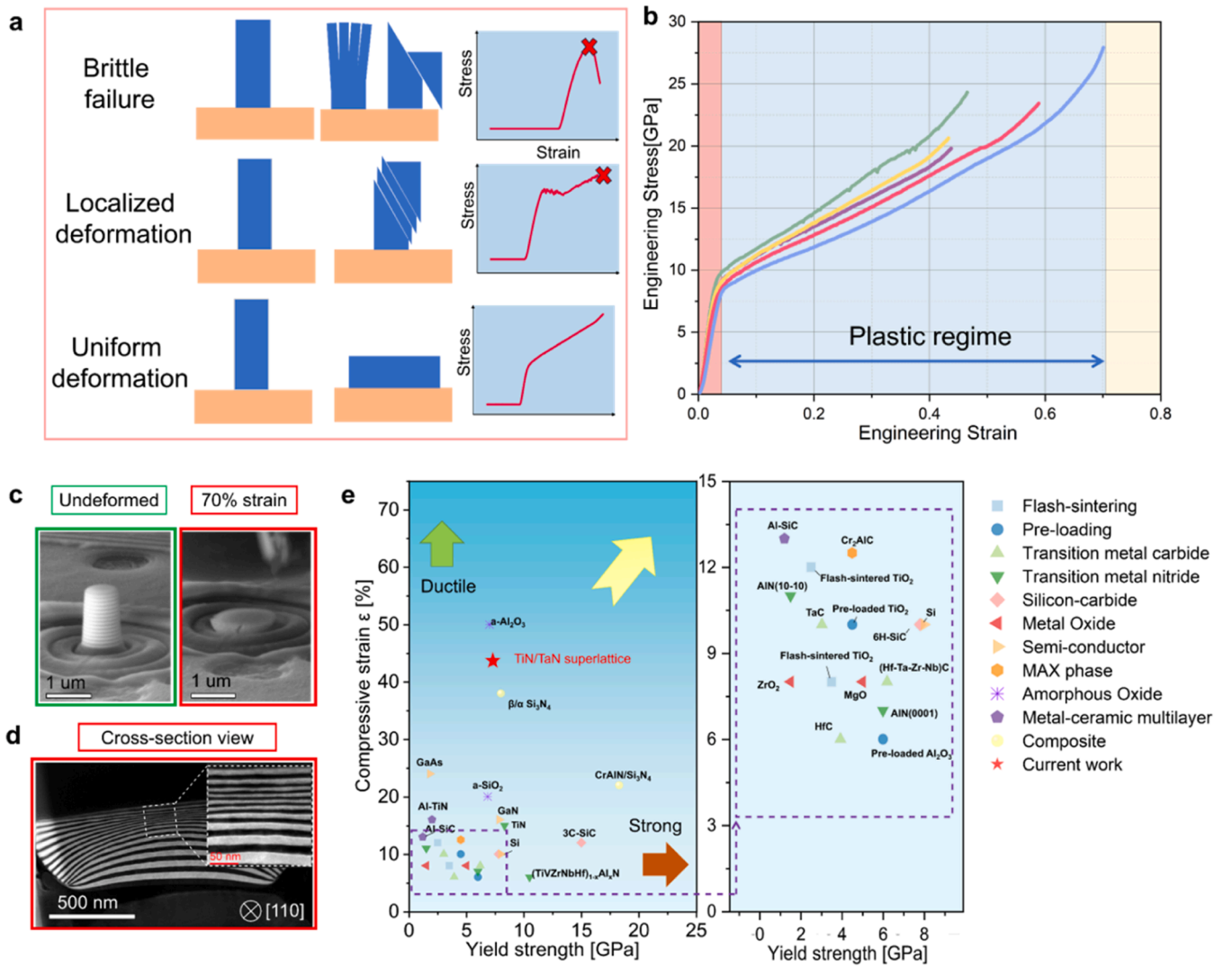
Fig. 4. Superior room-temperature plasticity of TiN/TaN superlattice. (a) Representative engineering stress-strain curves for ceramic micro-pillars, in which red crosses indicate the failure. **(b)** Engineering stress-strain curves recorded during compression of TiN/TaN superlattice, after yielding at $\varepsilon_c = 0.2\%$, stress can increase with strain steadily until $\varepsilon_c \approx 70\%$ **(c)** SEM images of an undeformed pillar and its post-compression state with $\varepsilon_c \approx 70\%$. **(d)** Cross-section view HAADF STEM image of the compressed pillar with $\varepsilon_c \approx 70\%$ **(e)** Recently reported maximum strain without cracking and yield strength of ceramics and semiconductor materials measured by micropillar compression at room temperature. Detailed data can be found in Table 2, where the pillar size for each experiment has been included.

Table 1
Key mechanical parameters calculated from compression strain-stress curves.

Number	Compressive strain (%)	Yield Strength (GPa)	Young's Modulus
Pillar 1	46.5	8.28	387.7
Pillar 2	43.8	7.32	359.69
Pillar 3	43.3	7.39	362.18
Pillar 4	58.9	6.61	333.32
Pillar 5	70	7.79	267.4
Average	–	7.48±0.62	342.06±46

layer. Previous studies about introducing metallic phases as dislocation sources have proved an effective method to promote the synergetic deformation and the plasticity of brittle phases in the composite system [81,82]. However, metal layers usually have a large strength gap with the ceramic phase, which can cause early failure at the interfaces before the plastic deformation of the brittle phases. However, TaN, as a transition metal nitride itself, overcomes the shortcoming. The closer strength and good strengthening ability make it more suitable for dislocation multiplication. On the other hand, the de-accumulation of gliding dislocations inside TiN layers prevents the stress concentration

and early-stage crack formation. The co-deformation of the TiN/TaN superlattice exhibited interesting inhomogeneity. To clarify the dislocation behaviors across the superlattice, we performed **g·b** diffraction contrast analysis by TEM on the compressed pillar sample strained to 20% (Fig. 8a - d). Based on the invisibility rule of dislocations when **g·b** = 0, Burgers vector **b** can be determined. Although both layers experienced about 20% compressive strain, abundant dislocations concentrate in TaN, while few appear in TiN. As marked by arrows in Fig. 8a - d, $[\overline{1}0\overline{1}]$ and $[10\overline{1}]$ dislocation arrays slide across the TaN layer while $[1\overline{1}0]$ dislocations remain inside TiN. The missing a/2<101> dislocations can only be rationalized by that they have moved across the interfaces to enter the adjacent TaN layers. Considering that TiN and TaN share the same crystallographic structure and a nearly perfect interface, <101> {101}dislocations can cross the interfaces with less resistance. This helps reduce the dislocation accumulation inside TiN, and activating <101>{110} dislocations provides extra plasticity for TaN. Meanwhile, a dense planar defect network limits the gliding of these dislocations (Fig. 8e). For instance, parallel SFs pin the gliding dislocation arrays, leaving the dislocation bowing out. Because the distance between adjacent SFs is only a few nanometers, dislocation glide becomes
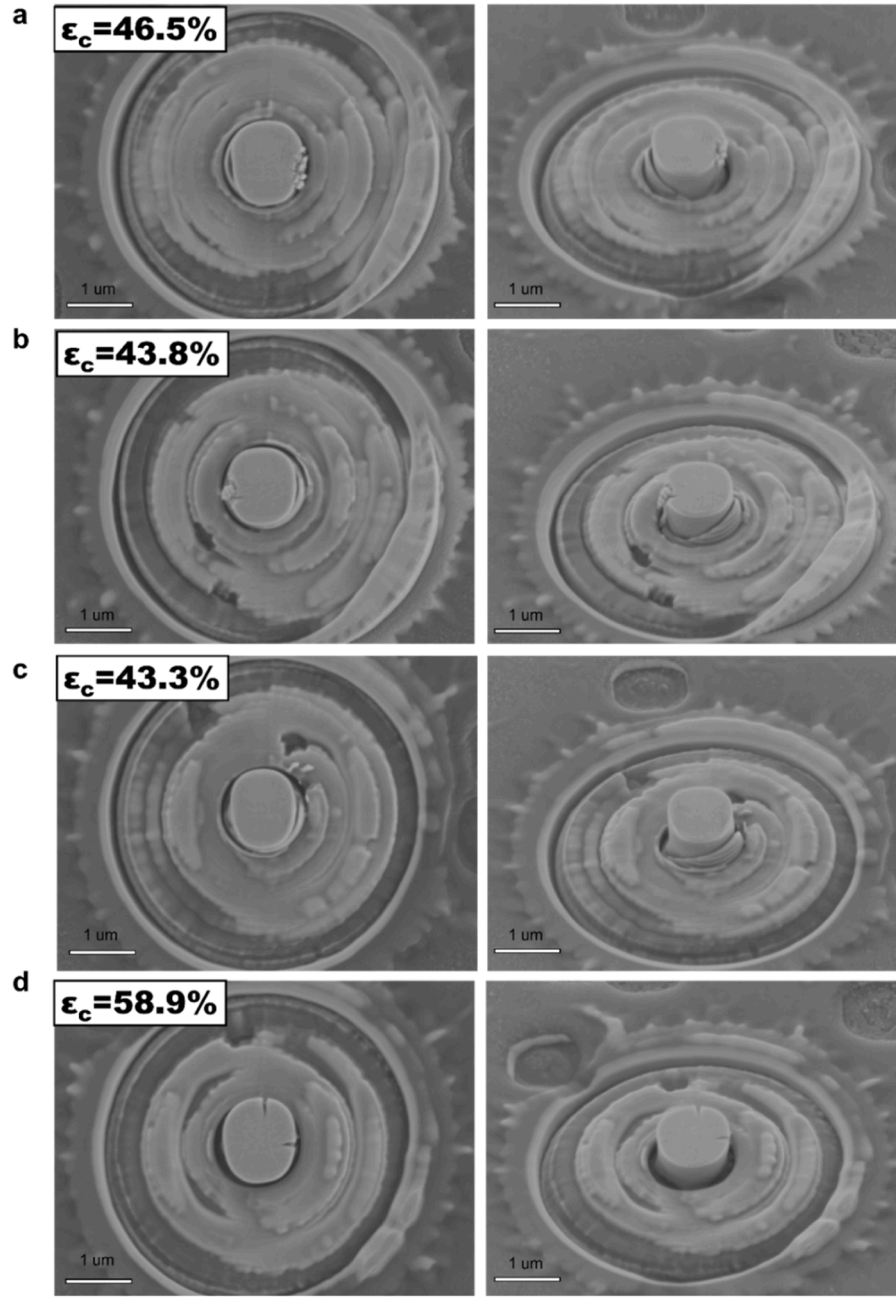
Fig. 5. SEM images of post-compression micro-pillars with different strains. (a) Pillar 1 strained to 46.5%. **(b)** Pillar 2 strained to 43.8%. **(c)** Pillar 3 strained to 43.3%. **(d)** Pillar 4 strained to 58.9%.

confined, making entanglement difficult. Additionally, the sessile dislocations resulting from the intersected SFs can stop dislocations from subsequent gliding. As a result, dislocations induced by the deformation of TiN are collected by TaN, helping reduce the dislocation accumulation in TiN and thus providing extra plasticity and strain hardening for TaN. The disconnection of <101>{101}dislocation gliding also explains the lacks of continuous shearing bands after the deformation, this prevents the macroscopic deformation localization.

3.5. Schmid factor and slip systems analysis

We confirmed that $\langle 11\bar{2}\rangle$ {111} slip systems were activated and dominant in TaN deformation at room temperature. The negative SFE promotes the dissociation of perfect dislocations into partial dislocations, bypassing the <101>{101} slip consequently. Considering the coupling between the perfect dislocation and its dissociative partial dislocations, the number of active slip systems for $\langle 11\bar{2}\rangle$ {111} and <101>{111} is the same. If we assume that the loading direction is along $[00\bar{1}]$ direction as micropillar compression tests, the operation of {111} slip allows for more slip systems compared to {101} slip (as shown in Fig. 9). There are four {111} planes and each plane have three $\langle 112\rangle$ directions, leading to 12 possible slip systems. The deformation of a single crystalline should consider Schmid factor, and the Schmid factor (m) can be calculated using the formula:

m=cos(φ)cos(λ)

Where: φ is the angle between the slip plane normal (**n**) and the loading direction. λ is the angle between the slip direction (**d**) and the loading direction.

For the (111) plane, normalized slip plane normal $\boldsymbol{n} = \frac{1}{\sqrt{3}}(1,1,1)$.
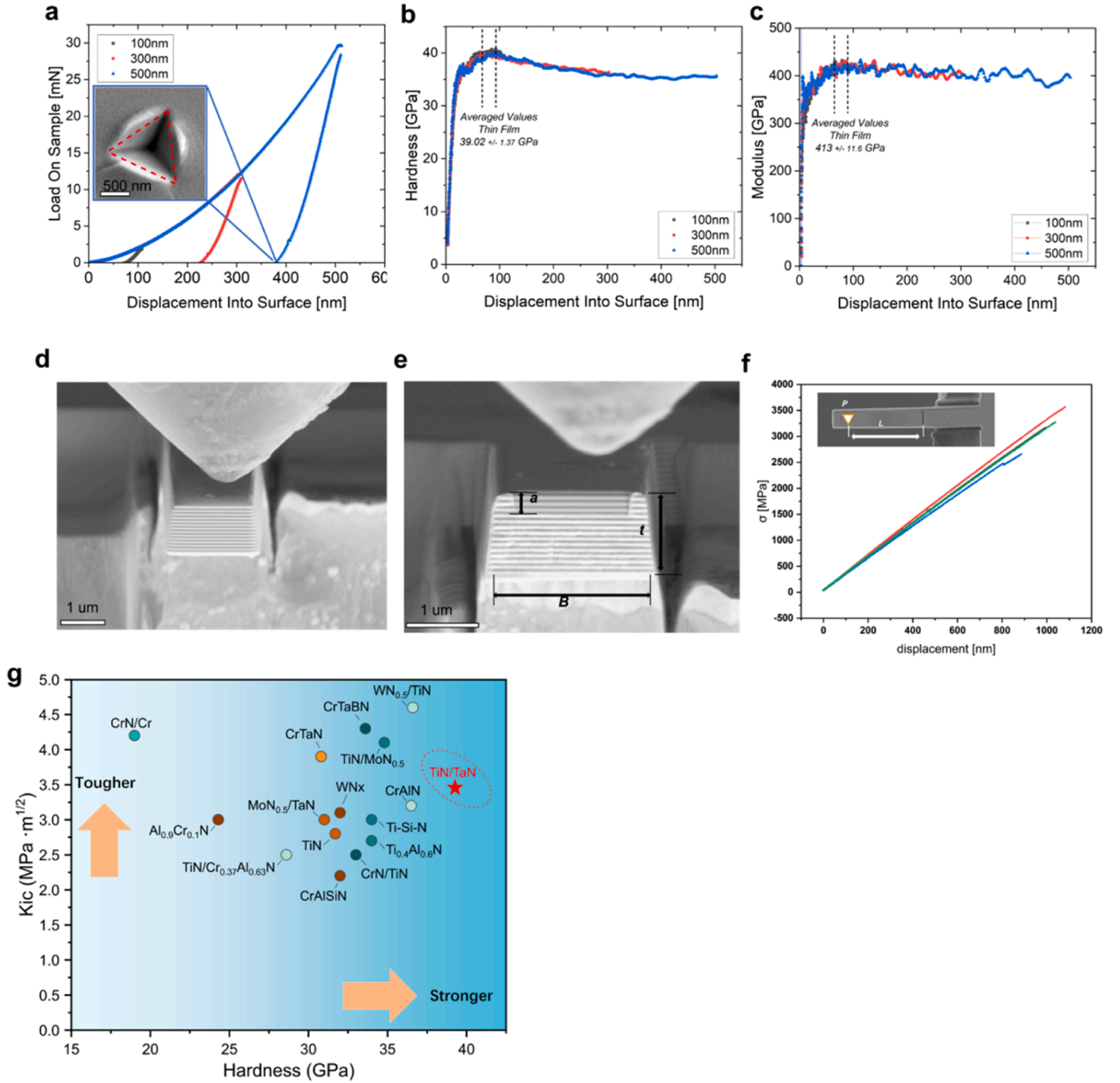
Fig. 6. Nanoindentation and micro-cantilever bending tests for TiN/TaN superlattice. (a) Load-displacement curves of TiN/TaN superlattice with different indentation depths, the inset shows the residual impression with an indentation depth of about 500 nm. **(b)** Hardness, and **(c)** Elastic modulus variation of TiN/TaN superlattice with indentation depth. **(d)** Free-standing cantilever bending of TiN/TaN before fracture. **(e)** Cross-sectional fracture surface morphology of a cantilever, different cantilever geometric parameters are marked. **(f)** Load-deflection curves recorded during in situ bending tests on notched cantilevers, the inset represents the top-view geometry of the cantilever. **(g)** Ashby plot of hardness and fracture toughness relationship for different TMNs and TMN superlattices, detailed data can be found in Table 3.

There are three slip directions $[1\bar{1}0]$, $[01\bar{1}]$, and $[10\bar{1}]$. The Schmid factors for $[01\bar{1}]$ and $[10\bar{1}]$ are both $-\frac{1}{\sqrt{6}}$ while the Schmid factor for $[1\bar{1}0]$ is 0. Thus, there are eight active slip directions in [83] slip when loading is along $[00\bar{1}]$. Similarly, if the slip is on {110}, there are four possible slip directions with a non-zero z-components that make the Schmid factor non-zero. As a result, the number of slip systems realizes expansion.

3.6. Toughening mechanism and crack propagation of TiN/TaN

The distinct deformation mechanism also manifests in the crack propagation across the TiN/TaN superlattice interface. As depicted in Fig. 10a, the crack path in TaN is notably longer than that in TiN. Angle measurement between the crack and the interface in TaN ranged from 20° to 54°, whereas in TiN, these angles were much larger, with some nearly vertical. This indicates deflection occurred when a crack enters TaN from TiN, contrasting with single crystal TiN/AlN superlattice where straight slip lines typically appear along the shearing direction [9, 84]. Furthermore, SF density dramatically increased near cracks. For example, the SF density of $5.74 \times 10^{15}/m^2$ at approximately 100 nm away from the crack quickly increased to $1.13 \times 10^{16}/m^2$ next to the crack (As shown in Fig. 10b). The formation of a denser SF network

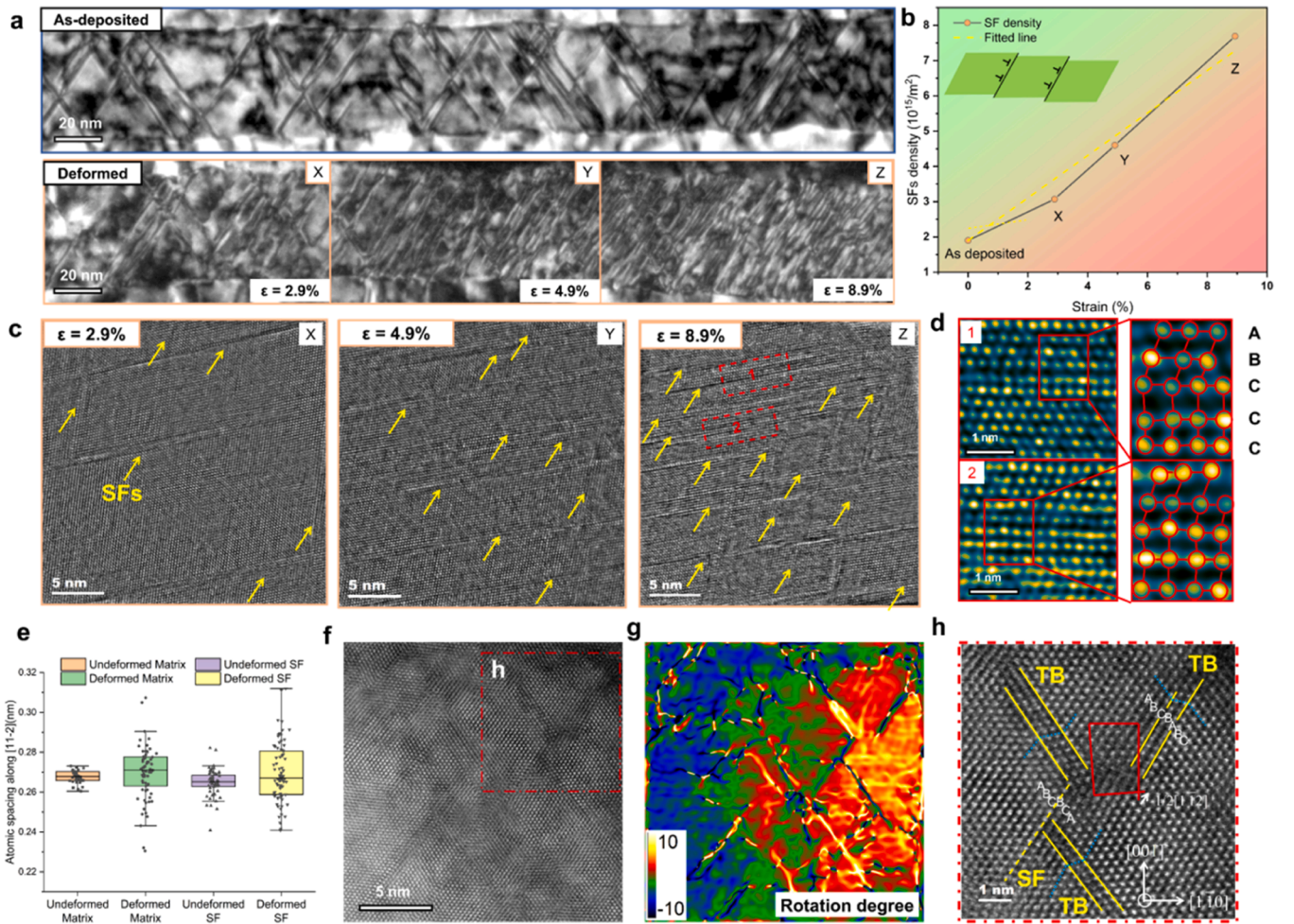**Fig. 7. Deformation mechanism of TaN. (a)** BF TEM images of as-deposited TaN and deformed TaN along [110] zone axis, **(b)** The monotonic relationship between SFs density and strain, **(c)** Atomic structure of SFs at region X, Y, Z, respectively, the magnified graph shows the atomic stacking sequence of SFs and the distortion. **(d)** magnified parts in region Z reveal the variation of Ta stacking orders. **(e)**The atomic spacing along $[11\bar{2}]$ direction in different regions of TaN. Deformation induces strong distortion in TaN. **(f)** HAADF STEM image of TaN layer with $\varepsilon_c \approx 30\%$, crossed partial dislocations divide the layer into smaller blocks, **(g)** geometric phase analysis rotation mapping indicates a rotation over 10 ° from left to right side across these block boundaries. **(h)** magnifies part of Fig. 7f reveals that some block boundaries consist of narrow twin bands or SFs.

effectively released the lattice strain. It dissipated the fracture energy at the crack tip [85]. Moreover, the high stress concentration near the crack tip triggered the development of twins (Fig. 10c, d). The emission of the SF network and twinning from the crack tip significantly contributed to crack tip blunting and toughening [85,86]. Besides, another crack shows similar characteristics in Fig. 10e, f. Because it is further away from the indentation impression, the crack length is far less than the one in Fig. 10a. The crack also experienced deflection when entering TaN. Meanwhile, the SF density near the crack tip is much higher than that of surrounding regions.

3.6.1. The impact of size effect

The size effect is a well-established phenomenon in micro- and nano-mechanical testing, wherein smaller sample dimensions often enhance plasticity [87]. A critical size typically exists for the brittle-to-ductile transition (BTDT) in brittle ceramics. For instance, silicon exhibits a critical diameter between 310 nm and 400 nm under uniaxial compression [88]. However, studies investigating BTDT in hard coatings are relatively scarce. This is primarily due to two challenges: the limited thickness of hard coatings constrains the dimensions of test pillars, and such materials often retain brittle characteristics even at the microscale [89]. For example, while TiN micro-pillars demonstrate some degree of room-temperature plasticity (~15%) at similar scales, they still exhibit

brittle fracture shortly after deformation begins [90]. In this work, we optimized the balance between diameter and aspect ratio to mitigate the size effect. As a result, TiN/TaN superlattices achieved over 40% plastic deformation without cracking at scales similar to those of TiN (refer to Table 2) and effectively resisted further brittle failure. While the size effect may contribute to the observed plasticity, we posit that it is not the primary factor responsible for the exceptional room-temperature plasticity of the TiN/TaN superlattice. In contrast, introducing TaN layer with intrinsic negative stacking fault energy and changing the deformation mechanism are more critical for the optimized mechanical properties.

4. Conclusions and perspective

With the growing recognition of the influence of defects on ceramic performance, ultra-dense planar defects brought by negative SFE endow transition metal nitrides ceramics with unique deformation mechanisms and lower threshold to plastic deformation. By combining with a multilayer structure, TiN/TaN exhibits superior room-temperature plasticity, toughness, and strength. Our study showcases the existence and feasibility of deformation-induced planar defects (e.g., SFs and twinning) in a TiN/TaN superlattice. Supported by experiments and theory studies, the reduction of energetic barriers for dislocation
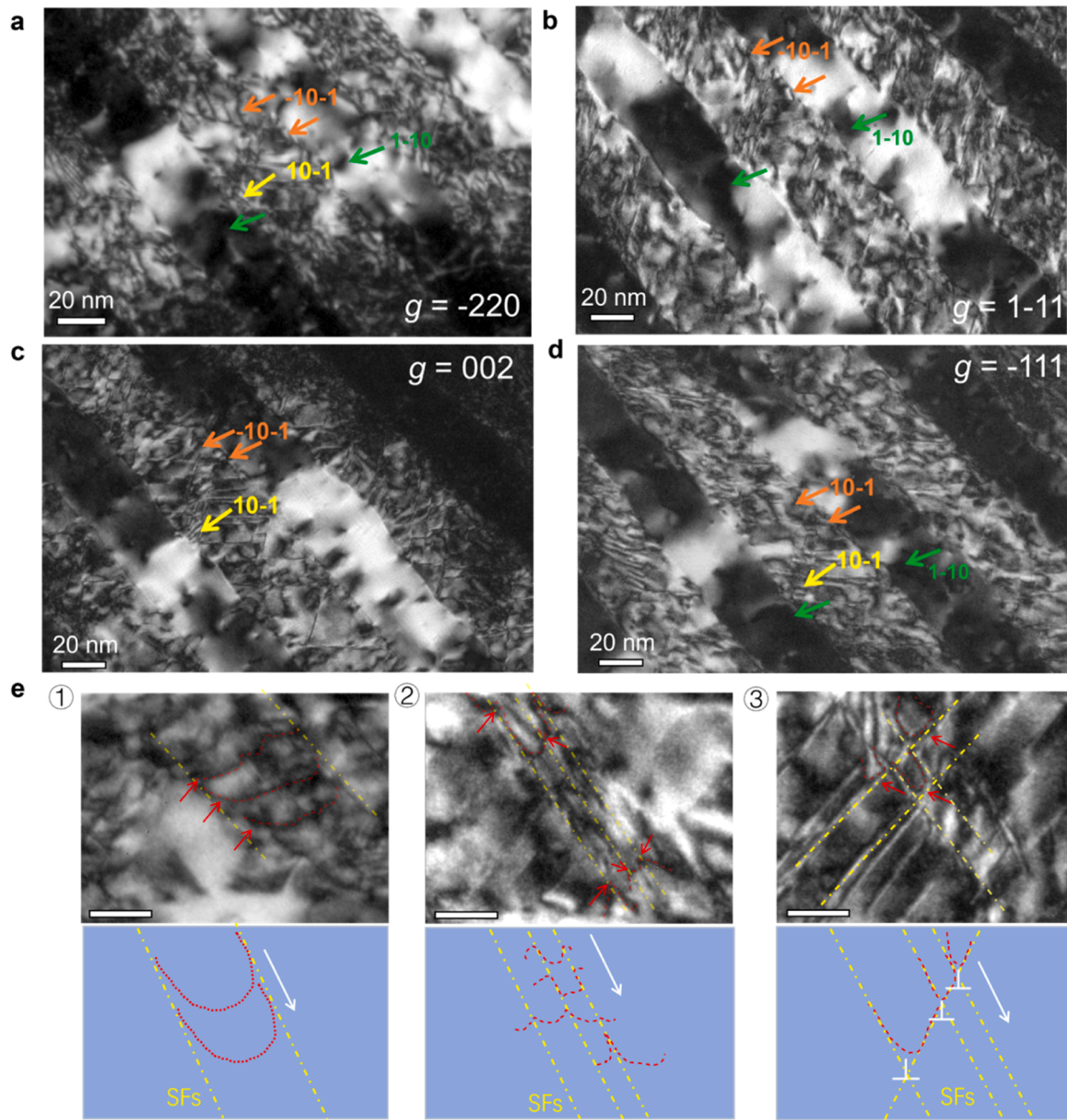
Fig. 8. Dislocation behavior and distribution in TiN/TaN superlattice. (a-d) Dark-Field TEM images with different **g** vectors exhibiting the dislocation distribution in TiN/TaN superlattice after compressive straining to 20%. (e) Schematics and magnified TEM images of interactions between dislocations and planar defects. ① wide parallel SFs confine the gliding of dislocations, ② relatively narrow SFs pin the intersections of dislocations, ③ sessile dislocations arrays stop the gliding of dislocations. Red curly lines indicate ⟨101⟩ dislocations, and yellow lines indicate SFs inside TaN(scale bar = 10 nm).
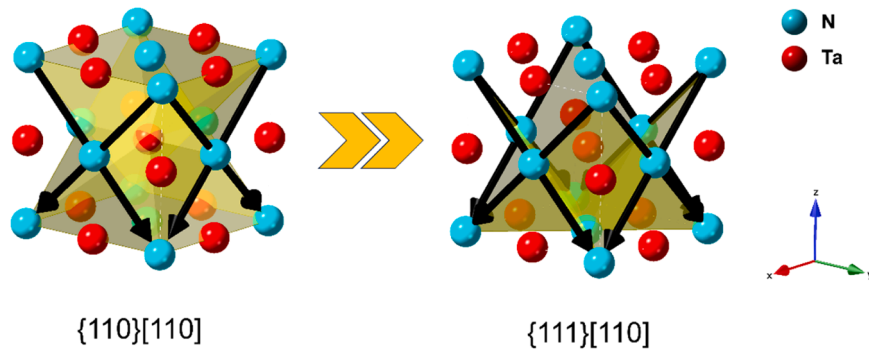

Fig. 9. Schematic of possible slip systems for ⟨110⟩{110} and ⟨110⟩{111}.
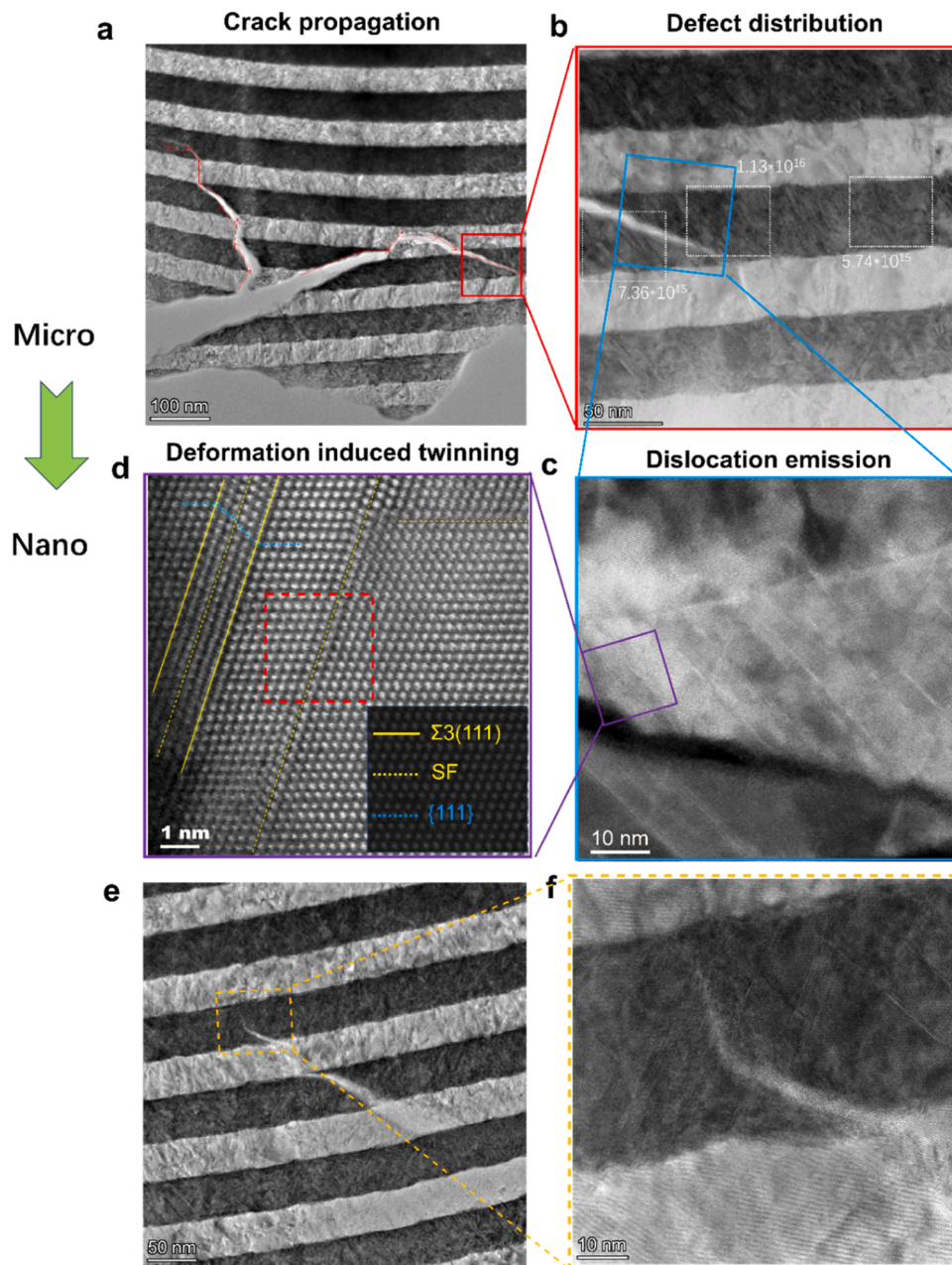
Fig. 10. Crack deflection and dislocation emission at crack tips in TiN/TaN superlattice (**a**) Overview of crack propagation at the plane side under the indentation impression, (**b**) local BF image near the crack tip (highlighted by red rectangle in Fig. 10a), (**c**) ADF image around the crack, (**d**) High-resolution HAADF image near the crack showing the atomic structure of deformation SFs and twins. (**e**) BF TEM image of a crack formed at the other side of the residual impression. (**f**) HRTEM image of the enlarged part near the crack, more successive SFs are on the left side.

nucleation and the expansion of active slip systems contribute to superior ductility. Moreover, the introduction of a ductile TaN layer promotes the co-deformation of the TiN/TaN superlattice and contributes to substantial strain hardening by interface strengthening.

This work advances the development of defect engineering in TMNs and other ceramics. The observation of abundant deformation SFs and twins shows the great potential of twinning-induced plasticity in ceramics. The distinctive attribute of negative SFE is shared by TMNs in the VB and VIB groups, as well as abundant potential high entropy nitrides. Further investigations into predicting and verifying these compounds are of great interest. Additionally, tuning SFE through alloying or vacancy regulation could further broaden the application spectrum and propel the design of novel ceramics for diverse applications.

CRediT authorship contribution statement

Yong Huang: Writing – original draft, Methodology, Investigation, Formal analysis, Conceptualization. **Zhuo Chen:** Writing – review & editing, Methodology. **Michael Meindlhumer:** Writing – review & editing, Methodology, Investigation. **Rainer Hahn:** Writing – review & editing, Methodology, Investigation, Formal analysis. **David Holec:** Writing – review & editing, Validation, Methodology, Investigation. **Thomas Leiner:** Writing – review & editing, Methodology, Investigation. **Verena Maier-Kiener:** Writing – review & editing, Methodology, Investigation, Formal analysis, Data curation. **Yonghui Zheng:** Writing – review & editing, Methodology, Investigation, Formal analysis. **Zequn Zhang:** Writing – review & editing, Visualization, Methodology, Investigation. **Lukas Hatzenbichler:** Writing – review & editing,

Table 2

A summary of yield strength and maximum strain measured by micro-pillar compression of recently reported ceramics and semiconductors.

System	Yield strength (GPa)	Maximum strain (%)	Pillar size (μm)	Reference
flash sintered TiO_2	2–2.5	12	~3	[51]
flash-sintered YTZ	3.5	8	~3	[13]
pre-loaded TiO_2	4.5	10	~3	[52]
pre-loaded Al_2O_3	6	6	~3	[52]
6H-SiC	7.8	10	0.28	[53]
HfC	3.93	6	~2.5	[54]
TaC	3.03	10	~2.5	[54]
(Hf-Ta-Zr-Nb)C	6.2	8	~2.5	[54]
GaAs	1.8	24	1	[55]
TiN/ZrN	8.5	4	~2	[56]
$(TiVZrNbHf)_{1-x}Al_xN$	10.5	6	~1.8	[57]
AlN(0001)	6	7	4	[58]
ZrO_2	1.5	8	1	[59]
AlN(10–10)	1.5	11	3	[58]
3C-SiC	15	12	0.65	[60]
Si	8	10	0.5	[61]
MgO(111)	5	8	0.5	[62]
GaN	7.85	16	~4	[63]
$β/α\ Si_3N_4$	8	38	0.35	[8]
TiN	~9	15	~1	[64]
Cr_2AlC	4.5	12.5	1.2	[65]
TS-BN	0.4	14	2700	[66]
$CrAlN/Si_3N_4$	18.3	22	0.38	[67]
Al–TiN	2	16	~5	[21]
Al-SiC	1.2	13	2	[68]
$a-Al_2O_3$	7	50	2.25	[10]
$a-SiO_2$	6.85	20	3.1	[50]
TiN/TaN	7.5	43.3	0.8	This work

Table 3

A summary of the experimentally measured hardness and fracture toughness of transition metal nitride coatings.

All summarized hardness and modulus data are derived from nanoindentation experiments. The fracture toughness of all thin films was unveiled by performing pre-notched single cantilever bending experiments of freestanding coating material.

System	Hardness (GPa)	K_{ic} (MPa$\sqrt{m}$)	Reference
$WN_{0.5}/TiN$	36.6	4.6	[69]
TiN(MgO-sub)	31.7	2.8	[69]
$TiN/Cr_{0.37}Al_{0.63}N$	28.6	2.5	[70]
$MoN_{0.5}/TaN$	31	3	[71]
CrN/TiN	33	2.5	[72]
$TiN/MoN_{0.5}$	34.8	4.1	[73]
WN_x	32	3.1	[69]
Ti-Si-N	34	3	[74]
CrAlN	36.5	3.2	[75]
CrAlSiN	32	2.2	[75]
$Ti_{0.4}Al_{0.6}N$	34	2.7	[76]
CrN/Cr	19	4.2	[77]
CrTaN	30.8	3.9	[78]
CrTaBN	33.6	4.3	[78]
$Al_{0.9}Cr_{0.1}N$	24.3	3	[79]
TiN/TaN	39.02±1.37	3.4 ± 0.5	this work

Methodology, Investigation. **Helmut Riedl:** Writing – review & editing, Methodology. **Christian Mitterer:** Writing – review & editing, Methodology, Data curation. **Zaoli Zhang:** Writing – review & editing, Supervision, Project administration, Methodology, Funding acquisition, Formal analysis, Data curation, Conceptualization.

Declaration of interests

The authors declare that they have no known competing financial interests or personal relationships that could have appeared to influence the work reported in this paper.

References

[1] W.D. Callister Jr, D.G. Rethwisch, Fundamentals of Materials Science and engineering: an Integrated Approach, John Wiley & Sons, 2020.

[2] J. Musil, Hard and superhard nanocomposite coatings, Surface Coat. Technol. 125 (1-3) (2000) 322–330.

[3] M. Cain, R. Morrell, Nanostructured ceramics: a review of their potential, Appl. Organometallic Chem. 15 (5) (2001) 321–330.

[4] J.P. Hirth, L. Kubin, Dislocations in Solids, Elsevier, 2009.

[5] N. Li, S. Yadav, X.-Y. Liu, J. Wang, R. Hoagland, N. Mara, A. Misra, Quantification of dislocation nucleation stress in TiN through high-resolution in situ indentation experiments and first principles calculations, Scient. Rep. 5 (1) (2015) 15813.

[6] G.W. Groves, A. Kelly, Independent slip systems in crystals, Philosoph. Magaz. 8 (89) (1963) 877–887.

[7] R.C. Garvie, R. Hannink, R. Pascoe, Ceramic steel?, Sintering Key Papers, Springer, 1990, pp. 253–257.

[8] J. Zhang, G. Liu, W. Cui, Y. Ge, S. Du, Y. Gao, Y. Zhang, F. Li, Z. Chen, S. Du, K. Chen, Plastic deformation in silicon nitride ceramics via bond switching at coherent interfaces, Science 378 (6618) (2022) 371–376.

[9] N. Koutná, L. Löfler, D. Holec, Z. Chen, Z. Zhang, L. Hultman, P.H. Mayrhofer, D. G. Sangiovanni, Atomistic mechanisms underlying plasticity and crack growth in ceramics: a case study of AlN/TiN superlattices, Acta Materialia 229 (2022) 117809.

[10] E.J. Frankberg, A. Lambai, J. Zhang, J. Kalikka, S. Khakalo, B. Paladino, M. Cabrioli, N.G. Mathews, T. Salminen, M. Hokka, J. Akola, A. Kuronen, E. Levänen, F. Di Fonzo, G. Mohanty, Exceptional microscale plasticity in amorphous aluminum oxide at room temperature, Adv. Mater. 35 (46) (2023) 2303142.

[11] Z. Chen, Y. Huang, N. Koutná, Z. Gao, D.G. Sangiovanni, S. Fellner, G. Haberfehlner, S. Jin, P.H. Mayrhofer, G. Kothleitner, Z. Zhang, Large mechanical properties enhancement in ceramics through vacancy-mediated unit cell disturbance, Nat. Commun. 14 (1) (2023) 8387.

[12] J. Li, J. Cho, J. Ding, H. Charalambous, S. Xue, H. Wang, X.L. Phuah, J. Jian, X. Wang, C. Ophus, Nanoscale stacking fault–assisted room temperature plasticity in flash-sintered TiO2, Science advances 5 (9) (2019) eaaw5519.

[13] J. Cho, Q. Li, H. Wang, Z. Fan, J. Li, S. Xue, K.S.N. Vikrant, H. Wang, T.B. Holland, A.K. Mukherjee, R.E. García, X. Zhang, High temperature deformability of ductile flash-sintered ceramics via in-situ compression, Nat. Commun. 9 (1) (2018) 2063.

[14] X. Fang, Mechanical tailoring of dislocations in ceramics at room temperature: a perspective, J. Am. Ceramic Soc. 107 (3) (2024) 1425–1447.

[15] X. Fang, A. Nakamura, J. Rödel, Deform to perform: dislocation-tuned properties of ceramics, American Ceramic Society Bulletin 102 (2023) 24–29.

[16] C. Okafor, K. Ding, X. Zhou, K. Durst, J. Rödel, X. Fang, Mechanical tailoring of dislocation densities in SrTiO3 at room temperature, J. Am. Ceramic Soc. 105 (4) (2022) 2399–2402.

[17] J. Matthews, A. Blakeslee, Defects in epitaxial multilayers: I. Misfit dislocations, J. Crystal Growth 27 (1974) 118–125.

[18] S. Jain, A. Harker, R. Cowley, Misfit strain and misfit dislocations in lattice mismatched epitaxial layers and other systems, Philosoph. Magaz. A 75 (6) (1997) 1461–1515.

[19] A. Misra, J. Hirth, H. Kung, Single-dislocation-based strengthening mechanisms in nanoscale metallic multilayers, Philosoph. Magaz. A 82 (16) (2002) 2935–2951.

[20] A.K. Mishra, H. Gopalan, M. Hans, C. Kirchlechner, J.M. Schneider, G. Dehm, B. N. Jaya, Strategies for damage tolerance enhancement in metal/ceramic thin films: lessons learned from Ti/TiN, Acta Material. 228 (2022) 117777.

[21] D. Bhattacharyya, N.A. Mara, P. Dickerson, R.G. Hoagland, A. Misra, Compressive flow behavior of Al–TiN multilayers at nanometer scale layer thickness, Acta Material. 59 (10) (2011) 3804–3816.

[22] L. Dong, J. Zhang, Y. Li, Y. Gao, M. Wang, M. Huang, J. Wang, K. Chen, Borrowed dislocations for ductility in ceramics, Science 385 (6707) (2024) 422–427.

[23] M. Soleimani, A. Kalhor, H. Mirzadeh, Transformation-induced plasticity (TRIP) in advanced steels: a review, Mater. Sci. Eng.: A 795 (2020) 140023.

[24] B.C. De Cooman, Y. Estrin, S.K. Kim, Twinning-induced plasticity (TWIP) steels, Acta Material. 142 (2018) 283–362.

[25] H. Huang, L. Shao, H. Liu, Stacking fault energies of high-entropy nitrides from first-principles calculations, Solid State Commun. 327 (2021) 114210.

[26] C.R. Weinberger, X.-X. Yu, H. Yu, G.B. Thompson, Ab initio investigations of the phase stability in group IVB and VB transition metal nitrides, Comput. Mater. Sci. 138 (2017) 333–345.

[27] M. Shih, J. Miao, M. Mills, M. Ghazisaeidi, Stacking fault energy in concentrated alloys, Nat. Commun. 12 (1) (2021) 3590.

[28] S. Wei, C.C. Tasan, Deformation faulting in a metastable CoCrNiW complex concentrated alloy: a case of negative intrinsic stacking fault energy? Acta Material. 200 (2020) 992–1007.

[29] P. Chowdhury, H. Sehitoglu, Deformation physics of shape memory alloys–fundamentals at atomistic frontier, Progr. Mater. Sci. 88 (2017) 49–88.

[30] S. Kibey, J. Liu, D. Johnson, H. Sehitoglu, Predicting twinning stress in fcc metals: linking twin-energy pathways to twin nucleation, Acta Material. 55 (20) (2007) 6843–6851.

[31] S. Lu, X. Sun, Y. Tian, X. An, W. Li, Y. Chen, H. Zhang, L. Vitos, Theory of transformation-mediated twinning, PNAS Nexus 2 (1) (2022).

[32] Y. Huang, Z. Chen, A. Wagner, C. Mitterer, K. Song, Z. Zhang, High density of stacking faults strengthened TaN/TiN multilayer, Acta Material. 255 (2023) 119027.

[33] W.C. Oliver, G.M. Pharr, An improved technique for determining hardness and elastic modulus using load and displacement sensing indentation experiments, J. Mater. Res. 7 (6) (1992) 1564–1583.

[34] H. Tada, P.C. Paris, G.R. Irwin, The stress analysis of cracks, Handbook, Del Res. Corpor. 34 (1973) (1973).

[35] H. Fei, A. Abraham, N. Chawla, H. Jiang, Evaluation of micro-pillar compression tests for accurate determination of elastic-plastic constitutive relations, (2012).

[36] J. Wheeler, J. Michler, Elevated temperature, nano-mechanical testing in situ in the scanning electron microscope, Rev. Scient. Instr. 84 (4) (2013).

[37] I.N. Sneddon, The relation between load and penetration in the axisymmetric Boussinesq problem for a punch of arbitrary profile, Int. J. Eng. Sci. 3 (1) (1965) 47–57.

[38] C.-S. Zha, H.-k. Mao, R.J. Hemley, Elasticity of MgO and a primary pressure scale to 55 GPa, Proc. National Acad. Sci. 97 (25) (2000) 13494–13499.

[39] G. Kresse, J. Furthmüller, Efficient iterative schemes for ab initio total-energy calculations using a plane-wave basis set, Phys. Rev. B 54 (16) (1996) 11169.

[40] G. Kresse, D. Joubert, From ultrasoft pseudopotentials to the projector augmented-wave method, Phys. Rev. B 59 (3) (1999) 1758.

[41] J.P. Perdew, K. Burke, M. Ernzerhof, Generalized gradient approximation made simple, Phys. Rev. Lett. 77 (18) (1996) 3865.

[42] H.J. Monkhorst, J.D. Pack, Special points for Brillouin-zone integrations, Phys. Rev. B 13 (12) (1976) 5188.

[43] D. Holec, P.H. Mayrhofer, Surface energies of AlN allotropes from first principles, Scripta Material. 67 (9) (2012) 760–762.

[44] Z. Chen, Y. Zheng, L. Löfler, M. Bartosik, H. Sheng, C. Gammer, D. Holec, Z. Zhang, Real-time atomic-resolution observation of coherent twin boundary migration in CrN, Acta Material. 208 (2021) 116732.

[45] S. Yadav, X.-Y. Liu, J. Wang, R. Ramprasad, A. Misra, R. Hoagland, First-principles density functional theory study of generalized stacking faults in TiN and MgO, Philosoph. Magaz. 94 (5) (2014) 464–475.

[46] N. De Leon, X.-x. Yu, H. Yu, C.R. Weinberger, G.B. Thompson, Bonding effects on the slip differences in the $B1$ monocarbides, Phys. Rev. Lett. 114 (16) (2015) 165502.

[47] H. Yu, M. Bahadori, G.B. Thompson, C.R. Weinberger, Understanding dislocation slip in stoichiometric rocksalt transition metal carbides and nitrides, J. Mater. Sci. 52 (11) (2017) 6235–6248.

[48] N. Koutná, D. Holec, O. Svoboda, F.F. Klimashin, P.H. Mayrhofer, Point defects stabilise cubic Mo-N and Ta-N, J. Phys. D 49 (37) (2016) 375303.

[49] M. Lebyodkin, Y. Brechet, Y. Estrin, L. Kubin, Statistics of the catastrophic slip events in the Portevin–Le Châtelier effect, Phys. Rev. Lett. 74 (23) (1995) 4758.

[50] R. Lacroix, G. Kermouche, J. Teisseire, E. Barthel, Plastic deformation and residual stresses in amorphous silica pillars under uniaxial loading, Acta Material. 60 (15) (2012) 5555–5566.

[51] J. Li, J. Cho, J. Ding, H. Charalambous, S. Xue, H. Wang, X.L. Phuah, J. Jian, X. Wang, C. Ophus, T. Tsakalakos, R.E. García, A.K. Mukherjee, N. Bernstein, C. S. Hellberg, H. Wang, X. Zhang, Nanoscale stacking fault–assisted room temperature plasticity in flash-sintered TiO2, Sci. Adv. 5 (9) (2019) eaaw5519.

[52] C. Shen, J. Li, T. Niu, J. Cho, Z. Shang, Y. Zhang, A. Shang, B. Yang, K. Xu, R. E. García, Achieving room temperature plasticity in brittle ceramics through elevated temperature preloading, Sci. Adv. 10 (16) (2024) eadj4079.

[53] S. Kiani, K.W.K. Leung, V. Radmilovic, A.M. Minor, J.M. Yang, D.H. Warner, S. Kodambaka, Dislocation glide-controlled room-temperature plasticity in 6H-SiC single crystals, Acta Material. 80 (2014) 400–406.

[54] T. Csanádi, E. Castle, M.J. Reece, J. Dusza, Strength enhancement and slip behaviour of high-entropy carbide grains during micro-compression, Scient. Rep. 9 (1) (2019) 10200.

[55] J. Michler, K. Wasmer, S. Meier, F. Östlund, K. Leifer, Plastic deformation of gallium arsenide micropillars under uniaxial compression at room temperature, Appl. Phys. Lett. 90 (4) (2007).

[56] L. Yang, Y. Chen, J. Chen, C. Wang, G. He, Anisotropic deformation and fracture mechanisms of physical vapor deposited TiN/ZrN multilayers, Ceram. Int. 46 (10) (2020) 15502–15509.

[57] A.V. Pshyk, A. Vasylenko, B. Bakhit, L. Hultman, P. Schweizer, T.E.J. Edwards, J. Michler, G. Greczynski, High-entropy transition metal nitride thin films alloyed with Al: microstructure, phase composition and mechanical properties, Mater. Des. 219 (2022) 110798.

[58] J.J. Guo, K.Madhav Reddy, A. Hirata, T. Fujita, G.A. Gazonas, J.W. McCauley, M. W. Chen, Sample size induced brittle-to-ductile transition of single-crystal aluminum nitride, Acta Mater. 88 (2015) 252–259.

[59] A. Lai, Z. Du, C.L. Gan, C.A. Schuh, Shape memory and superelastic ceramics at small scales, Science 341 (6153) (2013) 1505–1508.

[60] C. Shin, H.-H. Jin, W.-J. Kim, J.-Y. Park, Mechanical properties and deformation of cubic silicon carbide micropillars in compression at room temperature, J. Am. Ceramic. Soc. 95 (9) (2012) 2944–2950.

[61] M. Chen, L. Pethö, A.S. Sologubenko, H. Ma, J. Michler, R. Spolenak, J.M. Wheeler, Achieving micron-scale plasticity and theoretical strength in Silicon, Nat. Commun. 11 (1) (2020) 2681.

[62] S. Korte, W.J. Clegg, Discussion of the dependence of the effect of size on the yield stress in hard materials studied by microcompression of MgO, Philosoph. Magaz. 91 (7-9) (2011) 1150–1162.

[63] J.M. Wheeler, C. Niederberger, C. Tessarek, S. Christiansen, J. Michler, Extraction of plasticity parameters of GaN with high temperature, in situ micro-compression, Int. J. Plastic. 40 (2013) 140–151.

[64] G. Dehm, H.P. Wörgötter, S. Cazottes, J.M. Purswani, D. Gall, C. Mitterer, D. Kiener, Can micro-compression testing provide stress–strain data for thin films?: A comparative study using Cu, VN, TiN and W coatings, Thin Solid Film. 518 (5) (2009) 1517–1521.

[65] J. Yuan, S. Zhou, H. Wu, Z. Wang, Y. Zhang, G. Zhou, G. Ma, P. Ke, A. Wang, Ultrahigh strength-ductility of nanocrystalline Cr2AlC coating under micropillar compression, Scripta Material. 235 (2023) 115594.

[66] Y. Wu, Y. Zhang, X. Wang, W. Hu, S. Zhao, T. Officer, K. Luo, K. Tong, C. Du, L. Zhang, B. Li, Z. Zhuge, Z. Liang, M. Ma, A. Nie, D. Yu, J. He, Z. Liu, B. Xu, Y. Wang, Z. Zhao, Y. Tian, Twisted-layer boron nitride ceramic with high deformability and strength, Nature 626 (8000) (2024) 779–784.

[67] S. Liu, J.M. Wheeler, J. Michler, X.T. Zeng, W.J. Clegg, Plastic flow at the theoretical yield stress in ceramic films, Scripta Material. 117 (2016) 24–27.

[68] C.R. Mayer, L.W. Yang, S.S. Singh, J. Llorca, J.M. Molina-Aldareguia, Y.L. Shen, N. Chawla, Anisotropy, size, and aspect ratio effects on micropillar compression of AlSiC nanolaminate composites, Acta Material. 114 (2016) 25–32.

[69] J. Buchinger, N. Koutná, Z. Chen, Z. Zhang, P.H. Mayrhofer, D. Holec, M. Bartosik, Toughness enhancement in TiN/WN superlattice thin films, Acta Material. 172 (2019) 18–29.

[70] J. Buchinger, A. Wagner, Z. Chen, Z. Zhang, D. Holec, P.H. Mayrhofer, M. Bartosik, Fracture toughness trends of modulus-matched TiN/(Cr, Al) N thin film superlattices, Acta Material. 202 (2021) 376–386.

[71] R. Hahn, N. Koutná, T. Wójcik, A. Davydok, S. Kolozsvári, C. Krywka, D. Holec, M. Bartosik, P.H. Mayrhofer, Mechanistic study of superlattice-enabled high toughness and hardness in MoN/TaN coatings, Commun. Mater. 1 (1) (2020) 62.

[72] R. Hahn, M. Bartosik, R. Soler, C. Kirchlechner, G. Dehm, P.H. Mayrhofer, Superlattice effect for enhanced fracture toughness of hard coatings, Scripta Mater. 124 (2016) 67–70.

[73] Z. Gao, J. Buchinger, N. Koutná, T. Wojcik, R. Hahn, P.H. Mayrhofer, Ab initio supported development of TiN/MoN superlattice thin films with improved hardness and toughness, Acta Material. 231 (2022) 117871.

[74] M. Bartosik, R. Hahn, Z. Zhang, I. Ivanov, M. Arndt, P. Polcik, P. Mayrhofer, Fracture toughness of Ti-Si-N thin films, Int. J. Refractory Metal. Hard Mater. 72 (2018) 78–82.

[75] A. Drnovšek, H.T. Vo, M.R. de Figueiredo, S. Kolozsvári, P. Hosemann, R. Franz, High temperature fracture toughness of single-layer CrAlN and CrAlSiN hard coatings, Surface Coat. Technol. 409 (2021) 126909.

[76] M. Bartosik, C. Rumeau, R. Hahn, Z.L. Zhang, P.H. Mayrhofer, Fracture toughness and structural evolution in the TiAlN system upon annealing, Scient. Rep. 7 (1) (2017) 16476.

[77] A. Zeilinger, R. Daniel, M. Stefenelli, B. Sartory, L. Chitu, M. Burghammer, T. Schöberl, O. Kolednik, J. Keckes, C. Mitterer, Mechanical property enhancement in laminates through control of morphology and crystal orientation, J. Phys. D 48 (29) (2015) 295303.

[78] C. Kainz, M. Pohler, M. Tkadletz, C. Czettl, N. Schalk, The influence of bias voltage on structure, thermal stability and mechanical properties of arc evaporated Cr0.69Ta0.20B0.11N coatings, Surface Coat. Technol. 428 (2021) 127867.

[79] M. Meindlhumer, T. Ziegelwanger, J. Zalesak, M. Hans, L. Löfler, S. Spor, N. Jäger, A. Stark, H. Hruby, R. Daniel, Precipitation-based grain boundary design alters inter-to trans-granular fracture in AlCrN thin films, Acta Material. 237 (2022) 118156.

[80] N. Li, S.K. Yadav, X.Y. Liu, J. Wang, R.G. Hoagland, N. Mara, A. Misra, Quantification of dislocation nucleation stress in TiN through high-resolution in situ indentation experiments and first principles calculations, Scient. Rep. 5 (1) (2015) 15813.

[81] L.R. Dong, J. Zhang, Y.Z. Li, Y.X. Gao, M. Wang, M.X. Huang, J.S. Wang, K.X. Chen, Borrowed dislocations for ductility in ceramics, Science 385 (6707) (2024) 422–427.

[82] N. Li, H. Wang, A. Misra, J. Wang, In situ nanoindentation study of plastic Co-deformation in Al-TiN nanocomposites, Scient. Rep. 4 (1) (2014) 6633.

[83] G. Abadias, C.-H. Li, L. Belliard, Q.M. Hu, N. Greneche, P. Djemia, Large influence of vacancies on the elastic constants of cubic epitaxial tantalum nitride layers grown by reactive magnetron sputtering, Acta Material. 184 (2020) 254–266.

[84] Z. Chen, Y. Zheng, Y. Huang, Z. Gao, H. Sheng, M. Bartosik, P.H. Mayrhofer, Z. Zhang, Atomic-scale understanding of the structural evolution of TiN/AlN

superlattice during nanoindentation— Part 1: deformation, Acta Material. 234 (2022) 118008.

[85] P. Andric, The Mechanics of Crack-Tip Dislocation Emission and Twinning, EPFL, 2019.

[86] D.H. Warner, W.A. Curtin, S. Qu, Rate dependence of crack-tip processes predicts twinning trends in f.c.c. metals, Nat. Mater. 6 (11) (2007) 876–881.

[87] J.R. Greer, J.T.M. De Hosson, Plasticity in small-sized metallic systems: intrinsic versus extrinsic size effect, Progr. Mater. Sci. 56 (6) (2011) 654–724.

[88] F. Östlund, K. Rzepiejewska-Malyska, K. Leifer, L.M. Hale, Y. Tang, R. Ballarini, W. W. Gerberich, J. Michler, Brittle-to-ductile transition in uniaxial compression of silicon pillars at room temperature, Adv. Funct. Mater. 19 (15) (2009) 2439–2444.

[89] M.R. Schoof, J.S.K.L. Gibson, S. Karimi Aghda, M. Hans, J.M. Schneider, S. Korte-Kerzel, Orientation dependence of the fracture mechanisms in (V,Al)N coatings determined by micropillar compression, J. Mater. Res. 37 (4) (2022) 1003–1017.

[90] H. Wörgötter, D. Kiener, J.M. Purswani, D. Gall, G. Dehm, Testing thin films by microcompression: benefits and limits, BHM Berg- und Hüttenmännische Monatshefte 153 (7) (2008) 257–262.